1994-08-01

Role of Al2O3 particulate reinforcements on precipitation in 2014 Al-matrix composites

Dutta, I.; Dutta, G.; Harper, C.P.

Springer

Metallurgical Transactions, A (Physical Metallurgy and Materials Science); (United States); Journal Volume: 25:8
http://hdl.handle.net/10945/61017

A
Physical Metallurgy and Materials Science

METALLURGICAL AND MATERIALS TRANSACTIONS

Volume 25A–No. 8 August 1994 Pages 1557-1780

ASM INTERNATIONAL
TMS Minerals • Metals • Materials

Role of Al_2O_3 Particulate Reinforcements on Precipitation in 2014 Al-Matrix Composites

I. DUTTA, C.P. HARPER, and G. DUTTA

Precipitation in commercial aluminum alloy 2014, without and with alumina particulate reinforcements, was studied using microhardness, electrical resistivity, differential scanning calorimetry (DSC), and transmission electron microscopy. The precipitation sequence in 2014 Al was confirmed to be $\alpha_{ss} \rightarrow \alpha + GPZ \rightarrow \alpha + \lambda' \rightarrow \alpha + \lambda' + \theta' \rightarrow \alpha + \lambda$ (AlCuMgSi) + θ ($CuAl_2$). Reinforcement addition decreased the time to peak hardness, but also reduced the peak matrix microhardness. This was traced to a decrease in the amount of λ' formed in the composites. Further, it was observed that while Guinier–Preston (GP) zone and θ' formations are accelerated in the composites, λ' precipitation is decelerated. The acceleration is attributable primarily to enhanced nucleation resulting from an increase in the matrix dislocation density due to coefficient of thermal expansion (CTE) mismatch between the matrix and the reinforcements, whereas the deceleration is associated with a decrease of low-temperature solute diffusivity due to absorption of vacancies at dislocations and interfaces. It was also observed that the degree of overall acceleration in hardening and the reduction in peak matrix microhardness with reinforcement addition decreased with decreasing aging temperatures. The causal relationships of these observations with the associated mechanisms are discussed.

I. INTRODUCTION

AGING characteristics of discontinuously reinforced metal-matrix composites (MMCs) with precipitation-hardenable matrices have been widely reported to be accelerated relative to the unreinforced matrix alloy.[1–9] This behavior generally has been attributed to enhanced nucleation and growth due to the presence of high matrix dislocation densities around reinforcements. Matrix dislocations have been found to reduce the incubation time for heterogeneous nucleation of the strengthening precipitates,[6,8] as well as to increase solute diffusivity in the composite matrix.[8,10] Additionally, the elastic strain fields induced in the matrix because of the presence of reinforcements may promote stress-assisted solute diffusion, thereby accelerating precipitation in the composites with relatively low matrix dislocation density and/or large particle size.[5] Calorimetric studies on a number of MMC systems have shown that the addition of SiC to aluminum alloys does not alter the precipitation sequence of the matrix alloy, although precipitation kinetics are generally accelerated.[7] In addition to altering the kinetics, reinforcement addition has been observed to (a) alter the relative amounts of the precipitates formed;[8] (b) make some normally quench-insensitive materials quench-sensitive;[7] and (c) significantly alter the level of peak hardening obtained in the composite matrix relative to the unreinforced alloy.[1,3,8,11,12] While most studies indicate that the composite matrix hardens to a higher level than the unreinforced matrix, at least one instance of the composite matrix having a lower peak hardness has been reported.[11] This was attributed to a decreased vacancy concentration in the MMC matrix.

I. DUTTA, Associate Professor, and G. DUTTA, Adjunct Research Professor, are with the Department of Mechanical Engineering, Naval Postgraduate School, Monterey, CA 93943. C.P. HARPER, formerly Graduate Student, Department of Mechanical Engineering, Naval Postgraduate School, is currently with the United States Navy.

Manuscript submitted May 24, 1993.

Much of the literature on aging of composite matrices is based on powder metallurgy (PM) processed materials.[1,5–7,10] Although precipitation in cast alloys is slower than in PM processed materials,[7] cast SiC-Al composites have also been shown to exhibit accelerated aging.[9,12] A recent study of alumina-particulate-reinforced cast 6061 Al composites revealed accelerated aging relative to the monolith;[8] although the difference in the coefficient of thermal expansion between alumina and Al ($\sim 15 \times 10^{-6}$/K) is smaller than that between SiC and Al ($\sim 10 \times 10^{-6}$/K). So far, only one investigation of the aging behavior of 2014 Al in the presence of reinforcements (SiC) has been reported.[9] It found that reinforcements enhance the overall aging kinetics in 2014 Al at 195 °C but had little effect at 150 °C. The impact of reinforcements on each of the precipitation processes, however, was not studied in detail. To date, no study of the effect of Al_2O_3 reinforcements on the aging behavior of 2014 Al has been reported.

Despite the widespread use of Al-Cu-Mg-Si alloys in structural applications, little detailed information exists on precipitation in 2014 Al (nominally 4 pct Cu, 0.5 pct Mg, 0.8 pct Si). Crowther[13] first plotted the solidus of the Al-Cu-Mg-Si system and showed that for the composition regime corresponding to 2014 Al, the equilibrium phases are α, θ ($CuAl_2$), and a quaternary phase Q. Phagrem[14] analyzed this phase and concluded that it had the approximate chemical formula $Al_5Cu_2Mg_8Si_5$, had a hexagonal structure with lattice parameters of a = 10.30 Å and c = 4.04 Å, and grew in the form of hexagonal needles. The phase was later redesignated by Philips[15] as λ. In a study of Al-Cu-Mg-Si alloy (2x14 Al with 4.3 pct Cu, 0.87 pct Si, 0.53 pct Mg, and 0.006 pct Fe), Dubost *et al.*[16] presented electron-diffraction evidence that the peak-aged condition in these alloys consisted of θ' (transition $CuAl_2$) plates and needles of λ', a metastable form of the hexagonal phase λ. They[16] proposed that λ and λ' grow as needles along the $\langle 100 \rangle_{Al}$

directions with the orientation relationship (210) $\lambda' \parallel$ (100) Al and [100] $\lambda' \parallel$ [100] Al. It was suggested that in Al-Cu-Mg alloys with a significant amount of Si, the *S* phase (Al_2CuMg), found in alloys with low Si/Mg ratios, is replaced by the quaternary phase λ.

Based on the preceding, the purpose of this article is twofold: first, to establish the exact precipitation processes in 2014 Al, and second, to investigate the impact of alumina-particulate reinforcement on the precipitation behavior of a cast 2014 Al-matrix composite. Changes in microhardness and electrical resistivity of the MMC matrix have been monitored as functions of aging time and reinforcement volume fraction. Differential Scanning Calorimetry (DSC) and transmission electron microscope (TEM) investigations were also undertaken to characterize the sequence of precipitate evolution in the matrix alloy, and to observe the effect of reinforcements on each step in the precipitation sequence of 2014 Al.

II. EXPERIMENTAL PROCEDURE

The metal-matrix composites used in this work were commercial aluminum alloy 2014 reinforced with 10 and 15 vol pct Al_2O_3 particles. The materials were fabricated by Duralcan, Inc. (San Diego, CA) using a proprietary casting technique. After casting, the material was hot-extruded to homogenize the microstructure. The alumina reinforcement particles, which had aspect ratios of about one, had irregular shapes and ranged in size from about 1 to 22 μm. For comparison, unreinforced commercial 2014 Al in the cast and extruded forms was used as a control material. The chemical compositions of the control alloy and the composite matrices are given in Table I.

Microhardness measurements were conducted using a Buehler Micromet Tester equipped with a Vickers diamond pyramid indentor. Samples measuring 0.02 × 0.01 × 0.004 m were cut from the as-received stocks and were polished to a 1 μm finish. They were then solutionized at 793 K for 1.5 hours in a purified argon atmosphere and quenched in ice water at 273 K. Subsequently, the samples were aged at 458 K for various lengths of time and quenched to 273 K before hardness measurements were taken. Any interim storage before hardness testing was done in a freezer at 276 K. A minimum of six hardness readings were taken for each composite sample, with care being taken to avoid contact between the indentor and the reinforcement particles.

Table I. Composition of the Control Alloy and the Composites in Weight Percent

	2014 Al	10 vol pct MMC	15 vol pct MMC
Alumina	<0.01	12.66	20.65
Copper	4.57	4.27	3.95
Magnesium	0.42	0.37	0.27
Silicon	0.66	0.57	0.58
Iron	0.40	0.28	0.29
Manganese	0.77	0.71	0.70
Zinc	0.12	<0.005	<0.005
Titanium	0.04	0.009	0.008
Chromium	0.01	<0.01	<0.01
Aluminum	Balance	Balance	Balance

For the resistivity measurements, 0.115 × 0.038 × 0.018-m samples were machined from the as-received billets of the composite and the control alloy. Each sample was solutionized in argon atmosphere at 793 K and quenched to 273 K. Immediately thereafter, the sample was aged at either 313 ± 0.1 or 473 ± 0.1 K, and the electrical resistivity of the sample was monitored *in situ* using a standard four-point probe technique. The resistivity (ρ) data obtained from the tests were later converted into a matrix volume fraction (V_m) compensated relative resistivity change, $(1/V_m)$ $(\Delta\rho/\rho)$, to eliminate any effect of contact resistance and account for the difference of material volume undergoing transformation. Each test was repeated at least twice to ensure reproducibility.

In order to relate change in ρ to the phase transformations occurring in the matrix, thin foils of the monolith and the 10 vol pct Al_2O_3 MMC were examined using a TEM. 0.003-m-diameter disks were cut from the as-received stocks by electric discharge machining and were then ground mechanically to a thickness of about 30 μm using a TEM disk grinder. The samples were wrapped in aluminum foil, solutionized in inert atmosphere at 793 K for 1.5 hours, and quenched in ice water. They were then aged immediately for various lengths of time at either 313 or 473 K, quenched in ice water, and thinned to electron transparency. The unreinforced samples were thinned by electropolishing in a solution of 85 pct methanol and 15 pct nitric acid at 243 to 258 K using twin jets at a voltage of 20 V and a current of 25 mA. The composite samples were thinned in two steps. First, the disks were dimpled to a thickness of approximately 10 μm using 1 μm diamond paste in conjunction with a GATAN dimpler. In the second stage, the MMC disks were thinned using a GATAN duo-ion mill equipped with a liquid nitrogen cold stage at an accelerating voltage of 5 kV, a gun current of 1 mA, and a specimen-to-ion-beam inclination of 12 deg. All samples were examined using a JEOL* 100CX TEM at an accelerating voltage of 120 kV. Any storage between preparation and observation was done at 276 K. Samples in the solutionized and quenched states and those aged for short times or at low temperatures were examined immediately after preparation to avoid storage.

*JEOL is a trademark of Japan Electron Optics Ltd., Tokyo, Japan.

For the DSC experiments, 0.0015-m-thick disks of 0.0055-m diameter were machined from the as-received MMC and monolithic stocks by electric discharge machining. The disks were solutionized at 793 K for 1.5 hours in argon atmosphere and quenched in ice water at 273 K. They were then analyzed immediately in a PERKIN-ELMER* Series 7 DSC from 273 through 833 K at heating rates of 5, 10, or 20 K/min, using pure aluminum disks of the same mass as the reference. Some isothermal runs were also conducted. The heat-flow data

*PERKIN-ELMER is trademark of Perkin-Elmer Physical

from each run were converted to heat capacity (C_p) using a previously established calibration constant. Where needed, differential heat capacity (ΔC_p) *vs* T data were obtained by subtracting a baseline representing the C_p of the alloy with its existing precipitates, following the procedure described in Reference 8.

III. RESULTS

A. *Microhardness*

Figure 1 shows the variation of microhardness with aging time at 458 K for the control material and the two composites (10 and 15 vol pct). In the solution-treated condition, the composite matrices are observed to be harder than the monolith, suggesting an increased matrix dislocation density due to coefficient of thermal expansion (CTE) mismatch between the reinforcements and the monolith. While a large difference in hardness is noted between the monolith and the composite with 10 vol pct Al_2O_3, the difference in hardness between the 10 and 15 vol pct Al_2O_3 MMCs is small. This is consistent with an earlier study,[8] which found that increasing the reinforcement vol pct from 0 to 10 increases the mean dislocation density by about two orders of magnitude (from 3.1×10^{10} to 4.5×10^{12} m^{-2}), whereas a further increase from 10 to 15 leads to comparatively little additional increase (from 4.5×10^{12} to 7.3×10^{12} m^{-2}). The addition of alumina particulates also decreases the time required to achieve peak hardness from about 10 hours for the monolith to approximately 4 to 5 hours for the two composites. Relatively little acceleration is noted on increasing the reinforcement volume fraction from 10 to 15 pct, in agreement with the trend of dislocation density. Despite the acceleration, the level of peak hardness achieved in the composite matrices is observed to be appreciably less than the peak hardness of the unreinforced alloy, indicating that the overall gain in matrix strength achievable *via* heat treatment decreases with reinforcement addition. This is in contrast with most of the results reported to date,[3,4,8] which report the peak hardness to be higher in the presence of reinforcements. Friend and Luxton[11] reported a similar phenomenon in 6061 Al, where the addition of δ-alumina whiskers decreased the peak hardness of the composite, purportedly by absorption of vacancies needed for nucleation of (GP) zones at fiber-matrix interfaces. An examination of the results of Chawla *et al.*[9] reveals that the level of peak hardness achieved in a SiC/2014 Al composite at relatively high aging temperatures (453 and 468 K) was lower than those in the monolith, whereas at low aging temperatures (393 and 438 K), the opposite was true. They also reported that the aging kinetics of the composite are close to those of the monolith at low temperatures, but are greatly accelerated at higher aging temperatures.[9] Both observations are consistent with the results of this study, and will be rationalized later.

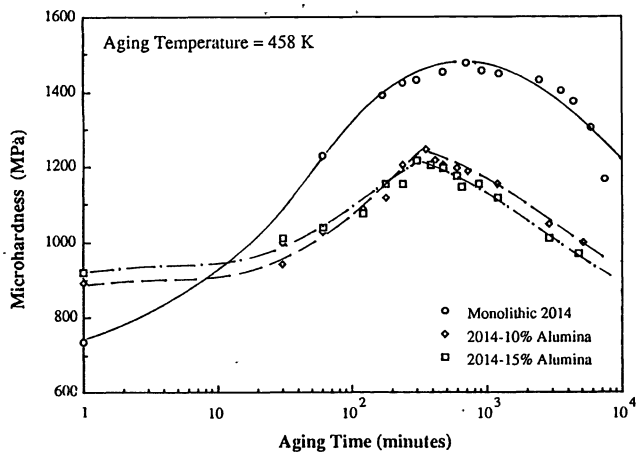

Fig. 1—Microhardness as a function of aging time at 458 K for the monolithic alloy and the two composites (10 and 15 vol pct). Alumina addition accelerates hardening but decreases peak hardness. Addition of 10 vol pct alumina has a large impact, with an additional 5 vol pct having little further impact.

B. *Calorimetry, Resistivity, and Transmission Electron Microscopy*

1. *Precipitation processes in 2014 Al*

Figure 2 shows a DSC thermogram of the unreinforced matrix alloy at a heating rate of 10 K/min, starting from the solution-treated condition. Three exothermic precipitation peaks, at (a) 350, (b) 507, and (c) 558 K are apparent, along with an endothermic dissolution peak at (d) 750 K. A less distinct, broad endothermic peak is also discernible between 430 and 490 K (e).

Figure 3 shows a centered dark-field TEM micrograph with $\mathbf{g}_{200}$ of a monolithic sample heated to 350 K and cooled rapidly to room temperature to reveal the precipitates corresponding to peak a. A mottled microstructure, revealing a high density of strain fields around tiny, unresolvable precipitates is observed. The corresponding $[001]_{Al}$ selected-area diffraction pattern (SADP) does not reveal any feature representative of the precipitates, suggesting that they are fully coherent with the matrix with ill-defined strain fields. These characteristics are representative of zone formation in Al-Cu-Mg alloys, with or without Si,[17,18,19] suggesting that peak a is associated with the formation of GP zones. Figure 4 shows the precipitates corresponding to peak b in a sample heated

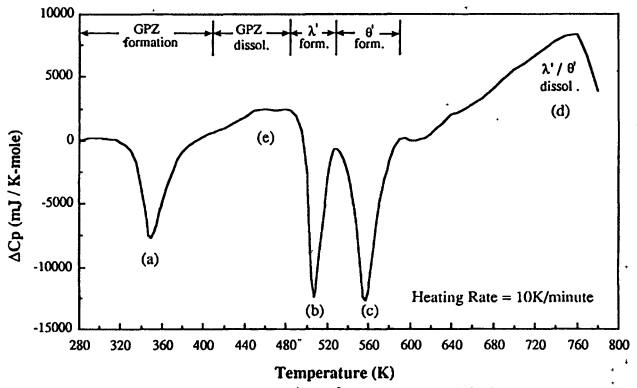

Fig. 2—DSC thermogram of the unreinforced matrix alloy at a heating rate of 10 K/min., starting from the solution-treated condition. The exothermic peaks are associated with (a) the formation of GP zone, (b) λ', and (c) θ', while the endotherms represent dissolution of (e) GP zones and (d) λ'/θ'.

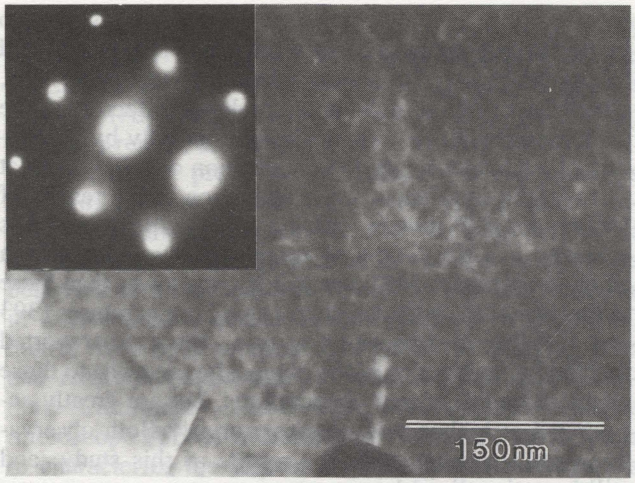

Fig. 3—Centered dark-field TEM micrograph with $\mathbf{g}_{200}$ and the corresponding $[001]_{Al}$ SADP of a 2014 Al sample, heated to 350 K at 10 K/min, revealing strain contrast due to tiny precipitates corresponding to peak a in Fig. 2.

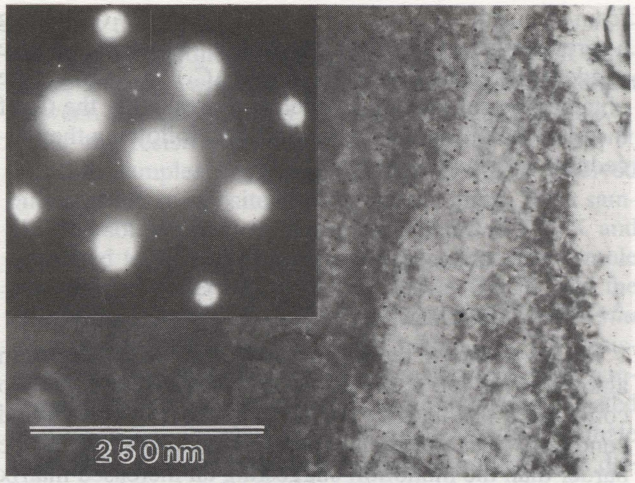

Fig. 4—Bright-field TEM micrograph of the monolith heated to 510 K at 10 K/min and rapidly cooled to reveal precipitates corresponding to peak b in Fig. 2. Needle-shaped precipitates oriented along $\langle 001 \rangle_{Al}$ are observed, with the $[001]_{Al}$ SADP identifying them as λ'.

to 510 K at 10 K/min and rapidly cooled. Numerous thin, needlelike precipitates oriented along $\langle 001 \rangle_{Al}$ are observed, along with many dots that are needles viewed end on. The corresponding SADP shows superlattice spots at 110_{Al} and faint streaks along $\langle 001 \rangle_{Al}$, identical to those reported for the λ' phase by Dubost *et al.*[16] Peak b, therefore, corresponds to λ' precipitation in 2014 Al. Figure 5 shows the microstructure of a sample heated to 560 K, corresponding to the middle of peak c. Precipitate plates are seen to have nucleated on matrix dislocations, with the SADP positively identifying them to be θ' (transition $CuAl_2$) according to analyses previously published.[20,21] The endothermic peaks e and d are due to the dissolution of the GP zones, and $\lambda' + \theta'$, respectively.

Thus, during a DSC scan, precipitation in 2014 Al begins with the precipitation of GP zones that nucleate either homogeneously or at quenched-in vacancy clusters, followed by zone dissolution around 440 to 480 K. The dissolving zones appear to act as nucleation sites for the λ' precipitates, which are evenly distributed throughout the matrix, just like the GP zones. On the other hand, θ' nucleates independently on matrix dislocations, its population density being significantly less than that of λ'.

Figure 6 illustrates the resistivity changes accompanying phase transformation in 2014 Al during isothermal aging at 473 K. A rapid rise in $(1/V_m)$ $(\Delta\rho/\rho)$ is observed to occur within the first 100 seconds of aging, followed by a drop till about 700 seconds. This is followed by a plateau up to 6000 seconds, and a final drop beyond that. These resistivity changes were characterized using DSC and TEM. The heat-flow data obtained from an isothermal DSC experiment at 473 K are superimposed on the resistivity data. The DSC data begin only after 120 seconds, since this time was necessary to equilibrate the DSC cell following rapid heating (400 K/min) of the sample from ambient to 473 K. It is clear from the DSC data that the drop in resistivity following the initial rise, and the subsequent plateau, correspond to

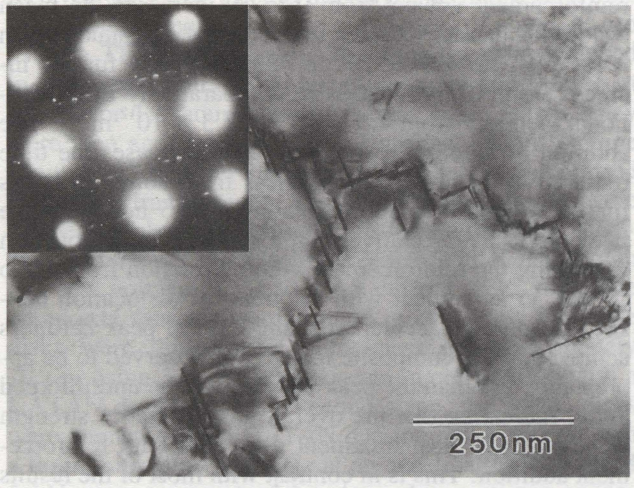

Fig. 5—TEM micrograph of the control alloy heated to 560 K, corresponding to peak c in Fig. 2. Platelike precipitates, which are identified as θ' (transition $CuAl_2$) by the SADP, are observed to have nucleated on dislocations.

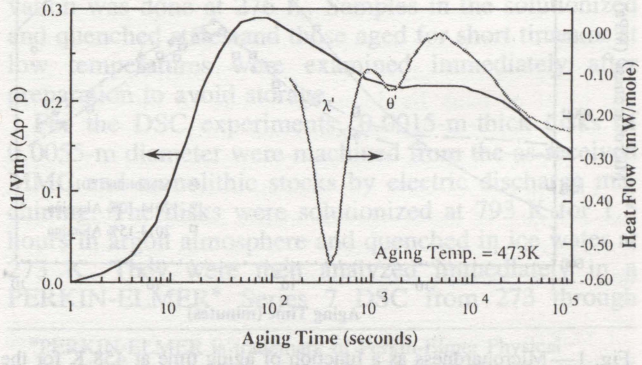

Fig. 6—Reinforcement volume fraction compensated resistivity changes, $(1/V_m)$ $(\Delta\rho/\rho)$, accompanying phase transformations in 2014 Al during isothermal aging at 473 K. Superimposed are heat-flow data from DSC, revealing the precipitation processes occurring during aging.

two different precipitation processes. The final resistivity drop is associated with a third, rather slow, precipitation process that may occur simultaneously as coarsening of the existing precipitates. Figure 7 shows a bright-field TEM image of the monolithic sample after aging at 473 K for 300 seconds. Three variants of very thin precipitate needles oriented along $\langle 100 \rangle_{Al}$ are observed to be distributed evenly throughout the matrix, with the SADP identifying them as λ'. Figure 8, which is a bright-field image of the $[001]_{Al}$ pole after 10,000 seconds at 473 K, reveals a coarser version of the needles observed in Figure 7, as well as numerous precipitate platelets that are situated on $[001]_{Al}$ and oriented along $\langle 100 \rangle_{Al}$. In addition to the pattern due to λ', the $[001]_{Al}$ SADP shows some sharpening of the $\langle 100 \rangle_{Al}$ streaks through the 110_{Al} positions, yielding a set of maxima corresponding to the phase θ' (compare with Figure 5). Further aging (to 14,400 seconds at 473 K) resulted in coarsening of the θ' platelets, as is clear from Figures 9(a) and 9(b), which show bright-field images of the $[001]_{Al}$ pole with the corresponding SADP, and of the sample tilted from the zone axis to reveal the precipitate plates. Based on the preceding, it can be concluded that the first drop following the initial rise in resistivity is due to the formation of a large amount of λ' precipitates, the following plateau is associated with the precipitation of a relatively small amount of θ' precipitates, whereas the final resistivity drop is due to the evolution of θ from θ', and possibly some coarsening of λ'. The initial rise in resistivity is attributable to the formation of GP zones, which increase electron scattering since their sizes are of the order of an electron wavelength, as well as because of the strain fields around them. It is likely that the zones start dissolving soon after forming since the aging temperature is very close to the solvus temperature for the zones (as suggested by the dissolution peak e in Figure 2), with the λ' precipitates nucleating from the dissolving zones.

2. *Comparison of precipitation in the monolith and the composites*

Figure 10 shows the DSC thermograms of the control alloy, the 10 vol pct Al_2O_3 composite, and the 15 vol

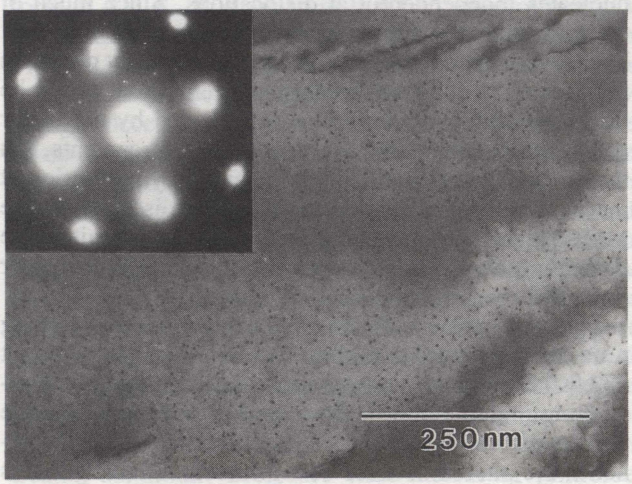

Fig. 7—Bright-field TEM micrograph and the corresponding SADP of monolithic 2014 Al aged for 300 seconds at 473 K, showing fine needlelike λ' precipitates.

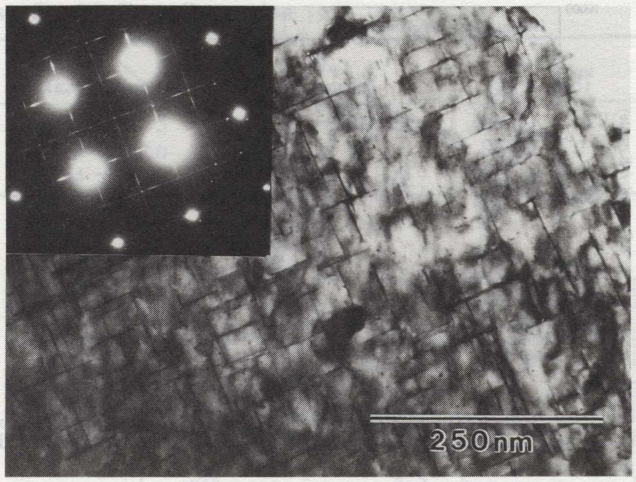

Fig. 8—Bright-field TEM micrograph and the corresponding SADP of monolithic 2014 Al aged for 10,000 seconds at 473 K, showing numerous θ' plates, as well as some coarse needles of λ'.

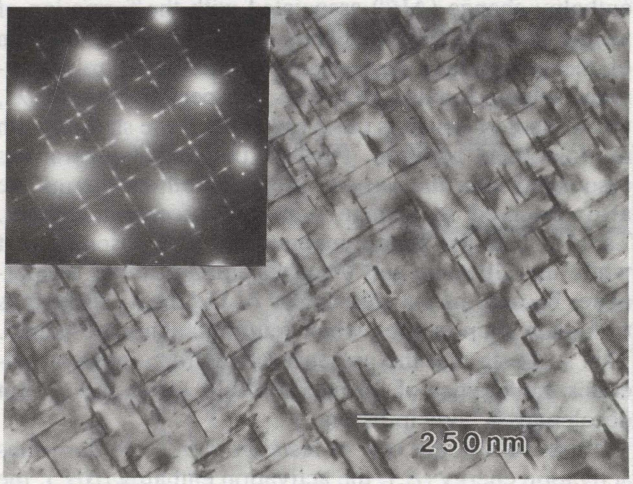

(*a*)

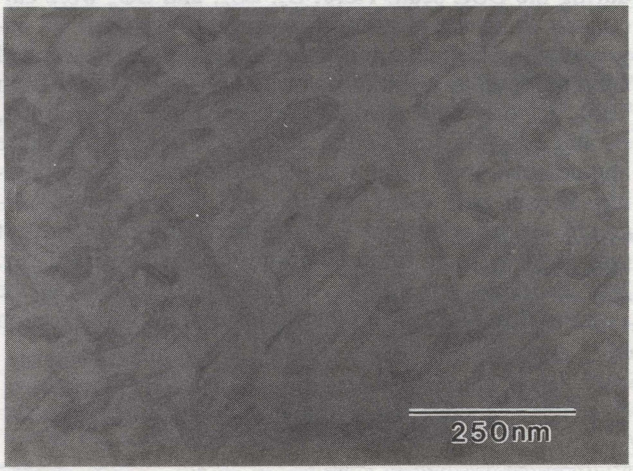

(*b*)

Fig. 9—(*a*) Bright-field TEM micrograph and the corresponding $[001]_{Al}$ SADP of 2014 Al aged for 14,000 seconds at 473 K, showing θ' plates. (*b*) Bright-field image of the same sample, tilted away from the zone axis to reveal the coarse precipitate plates.

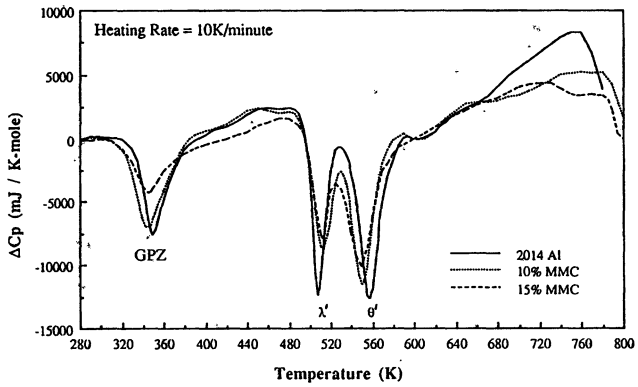

Fig. 10—DSC thermograms of the control alloy, the 10 vol pct Al_2O_3 composite, and the 15 vol pct Al_2O_3 composite after solutionizing and quenching, at a heating rate of 10 K/min.

pct Al_2O_3 composite after solutionizing and quenching, at a heating rate of 10 K/min. It is clear from Figure 10 that the addition of alumina reinforcements decreases the enthalpy change (ΔH_R) associated with the formation of all the precipitates, suggesting that the volume fraction of the precipitates decreases with increasing reinforcement volume fraction (V_f). This is especially true for λ', the amount of which is observed to decrease sharply with reinforcement addition. Further, the peak temperatures associated with the various precipitation exotherms are also observed to change with reinforcement content. Table II lists the peak temperatures. It is observed that while the GP zone and θ' peaks shift to lower temperatures because of the presence of Al_2O_3, the λ' peak shifts to higher temperatures when reinforcements are added. This suggests that the presence of reinforcements accelerates the kinetics of formation of GP zones and θ', but decelerates λ' precipitation.

Table III lists the heat of reaction (ΔH_R), the Arrhenius activation energy (E_a), the activation enthalpy (ΔH_a), the activation entropy (ΔS_a), and the free energy of activation (ΔG_a) associated with the formation of GP zones during the DSC scan. Here, E_a, ΔS_a, and ΔG_a were calculated using the absolute reaction rate theory,[22,23] approximating GP zone formation from the supersaturated solid solution as a first-order reaction. It is evident from Table III that with the addition of 10 vol pct alumina, E_a and ΔH_a, as well as the magnitude of ΔS_a, decrease appreciably, with only a small further decrease on adding 15 vol pct. Consequently, ΔG_a decreases significantly on the addition of 10 vol pct reinforcement, but only slightly more upon addition of a further 5 vol pct. It is also observed that the decrease in ΔG_a is about the same as that of E_a or ΔH_a, suggesting that the activation energy plays a more important role in determining ΔG_a than the activation entropy. Further, ΔH_R, and, therefore, the volume fraction of GP zones formed, clearly decrease with increasing reinforcement content.

Table II. Peak Temperatures of Precipitation Exotherms (K)

Material	GP Zone Formation	λ' Formation	θ' Formation
2014 Al	349.8	506.6	557.5
10 pct MMC	344.6	512.0	551.7
15 pct MMC	343.8	511.2	550.5

In the monolithic alloy, nucleation of GP zones occurs either homogeneously or on quenched-in vacancy loops. In the composite matrix, numerous dislocations are available for nucleation in addition to the quenched-in vacancies. The availability of the dislocations would therefore be expected to accelerate GP zone nucleation (by reducing incubation time, by enhancing nucleation rate, or both). The decrease in the overall activation energy (E_a), which incorporates the activation energies of both nucleation and growth, with reinforcement addition, reflects this. However, the dislocations and interfaces in the composite may also absorb vacancies, thus reducing the concentration of vacancies available for diffusion (and hence, growth). Following exhaustion of the existing vacancies, continued precipitation can occur only by solute diffusion. Since this has a larger activation barrier than vacancy diffusion, it is possible that the propensity to form GP zones (which are formed prior to the more mature precipitates primarily because they have a lower activation barrier) is stanched in the composites. This could explain the decrease in the volume fraction of GP zones precipitated with increasing reinforcement addition.

Table IV lists the activation energies (E_a) for λ' and θ' precipitation in the control material and the two composites, as calculated from the DSC results. Because of the partial superposition of the two peaks, the absolute reaction rate theory could not be used. Instead, E_a was calculated based on peak temperatures at varying heating rates following the method of Augis and Bennett.[24,25] As in the case of GP zone formation, a significant change in E_a is observed upon the addition of 10 vol pct alumina, with an additional 5 pct resulting in little further change. It is observed that E_a increases with reinforcement addition for λ' precipitation, but decreases with increasing V_f for θ' precipitation, suggesting that the presence of reinforcements assists θ' formation, but inhibits λ' precipitation. As indicated in Section III–B–1, λ' nucleates from the dissolving GP zones, whereas θ' nucleates independently at dislocations. Since much of the λ' precipitates form independently of dislocations (just like GP zones) and have to depend on vacancy diffusion for growth, a reduced vacancy concentration would be likely to inhibit λ' formation, as reflected by the larger activation barrier in the presence of reinforcements. On the other hand, θ' precipitation is aided by nucleation at matrix dislocations (the density of which is larger in the MMCs), and by enhanced growth *via* short-circuit solute diffusion down dislocation cores, resulting in the lower E_a in the composites.

Figure 11 plots $(1/V_m)$ $(\Delta\rho/\rho)$ as a function of aging time for the monolithic alloy and the two composites at 473 K. The basic nature of resistivity changes accompanying precipitation in the monolith and the composite are similar, although the degree of change and the kinetics are altered because of reinforcement change. It is apparent that the rise in resistivity commensurate with GP zone formation begins earlier in the composites. This is clearer in Figure 12(a), which plots the derivative of

Table III. Activation Constants for GP Zone Formation

Material	T_p (K)	ΔH_R (J/mole)	E_a (kJ/mole)	ΔH_a (kJ/mole)	ΔS_a (J/K mole)	ΔG_a (kJ/mole)
2014 Al	349.8	160	69.53 ± 8.33	66.61 ± 8.15	−96.61 ± 23.43	100.11 ± 2.2
10 pct MMC	344.6	149	66.56 ± 7.72	63.69 ± 7.56	−91.01 ± 22.1	96.42 ± 1.9
15 pct MMC	343.8	105	66.42 ± 8.8	63.54 ± 8.7	−90.65 ± 21.16	96.16 ± 2.1

Table IV. Activation Energy for λ' and θ' Precipitation

Material	E_a for λ' (kJ/mol)	E_a for θ' (kJ/mol)
2014 Al	80.167	82.031
10 pct MMC	88.476	73.455
15 pct MMC	88.586	72.589

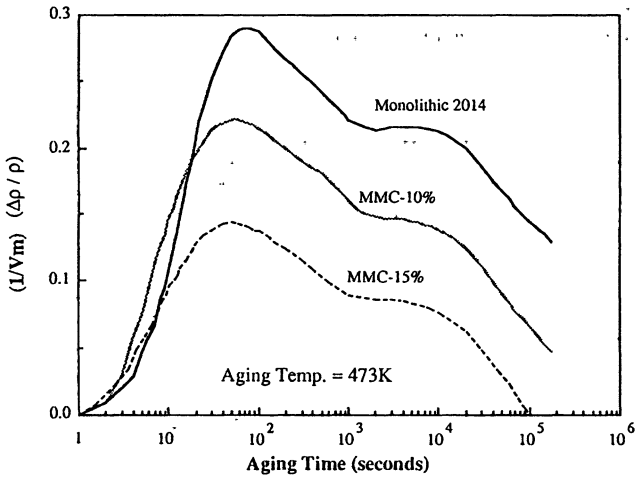

Fig. 11—Reinforcement volume fraction compensated change in resistivity, $(1/V_m)$ $(\Delta\rho/\rho)$, as a function of aging time for the monolithic alloy and the two composites at 473 K. The nature of resistivity changes accompanying precipitation in the monolith and the composite are similar, but the degree of change and the kinetics are different.

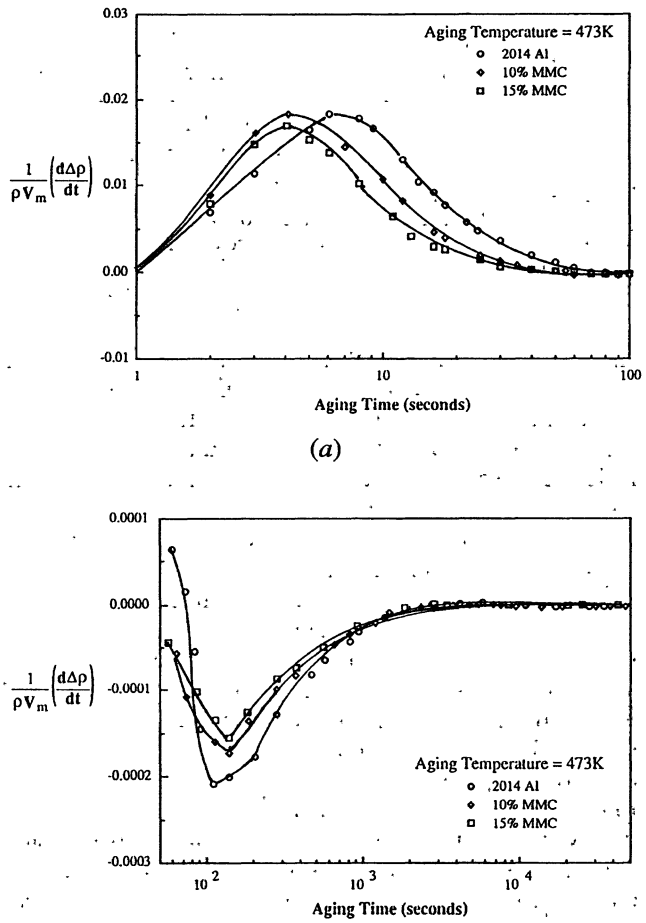

Fig. 12—(*a*) Time derivative of $(1/V_m)$ $(\Delta\rho/\rho)$ *vs* aging time at 473 K for the monolith and the composites up to 100 seconds, comparing the kinetics of GP zone formation. (*b*) Derivative of $(1/V_m)$ $(\Delta\rho/\rho)$ *vs* aging time at 473 K for the monolith and the composites beyond 100 seconds, comparing the kinetics of λ' formation.

$(1/V_m)$ $(\Delta\rho/\rho)$ *vs* aging time for the three materials up to 100 seconds, *i.e.*, the time within which GP zones form at 473 K. It is apparent that GP zone formation is accelerated in both composites relative to the monolith. Figure 12(b), which plots the derivative beyond the time required for GP zone formation, on the other hand, shows a slight deceleration in the kinetics of λ' formation because of reinforcement addition. The peak size, and hence, the volume fraction of λ' precipitates formed during isothermal aging at 473 K, clearly decrease upon the addition of alumina particulates. A close inspection of Figure 11 reveals that the duration of the plateau following the resistivity peak (corresponding to θ' formation) becomes shorter upon reinforcement addition, suggesting some acceleration of the precipitation kinetics of θ' in the presence of reinforcements. An additional feature to note in Figure 11 is that the overall change in volume fraction compensated resistivity, starting from the solution-treated condition, decreases with increasing reinforcement content. Since most of the resistivity rise is associated with GP zone formation, this may suggest that (1) reinforcements reduce the volume fraction of GP zones formed; or (2) the presence of reinforcements somehow reduces the coherency strains associated with the zones.

The impact of alumina reinforcements on the amount and kinetics of precipitation during aging at 473 K is better illustrated in Figure 13, which shows the heat flow measured by DSC as a function of aging time. Since DSC measures the heat associated with a reaction directly (as opposed to indirect techniques like resistivity measurement, which measures a property change due to precipitation), it is likely to yield better results, although data during the initial stages of aging are lost because of the requirement of equilibrating the cell following heating to the aging temperature. Confirming the results of resistivity measurements (Figure 12(b)), Figure 13 clearly

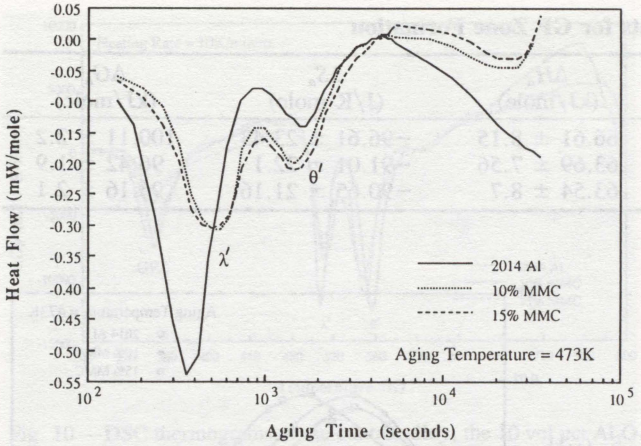

Fig. 13—Heat flow measured by DSC as a function of aging time at 473 K for monolithic 2014 Al and the two composites. Alumina addition reduces the amount of λ' while decelerating its kinetics, but increases the amount of θ' while enhancing its kinetics.

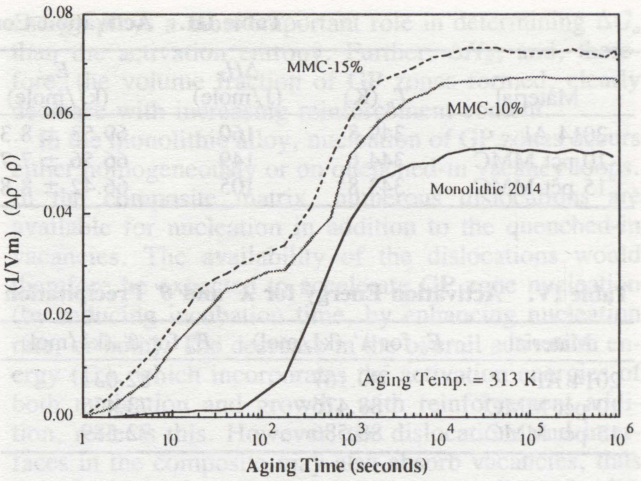

Fig. 14—Resistivity changes accompanying aging at 313 K, for the monolith and the two composites. A two-step resistivity rise with a very short incubation time is noted in the composites.

shows that reinforcement addition not only decelerates λ' precipitation, but reduces the volume fraction of λ' substantially. However, the volume fraction of θ' increases because of reinforcement addition, with its kinetics being somewhat accelerated. Finally, the coarsening of λ' and precipitation of θ from θ', which occur rather slowly in the monolith, are accelerated substantially in the composites, although the amount of θ formed appears to be relatively small in the composites.

The effect of reinforcement on the precipitation kinetics of GP zones is apparent from Figure 14, which shows the resistivity changes accompanying aging at 313 K. In the monolith, little change in resistivity is observed till about 100 seconds, beyond which the resistivity rises rapidly because of the formation of GP zones. In the composites, on the other hand, the resistivity rises with very little time required for incubation. A two-step rise in resistivity is noted, suggesting a two-stage precipitation process. As indicated earlier, matrix dislocations reduce incubation time, allowing precipitation to occur in detectable quantities even at short aging times. Following precipitation on the thermally generated matrix dislocations, nucleation occurs on quenched-in vacancy clusters. In the composites, both types of sites (*i.e.*, dislocations and vacancy clusters) are available for nucleation, accounting for the two-step process. In the monolith, on the other hand, the dislocation density is not adequate to result in detectable amounts of GP zone precipitation, resulting in a one-step precipitation of GP zones at vacancy clusters.

Figure 15 shows a bright-field TEM micrograph and the corresponding $[001]_{Al}$ SADP of the matrix of the composite with 10 vol pct Al_2O_3, aged for 300 seconds at 473 K. A fine distribution of λ' precipitates is observed, with its population density being significantly less than that in the monolith following the same aging treatment (compare with Figure 7). A comparison of the SADPs in Figures 15 and 7 also reveals that the precipitates in the composite are less mature than those in the monolith. Both observations are consistent with the resistivity and the DSC data, which indicated a reduction

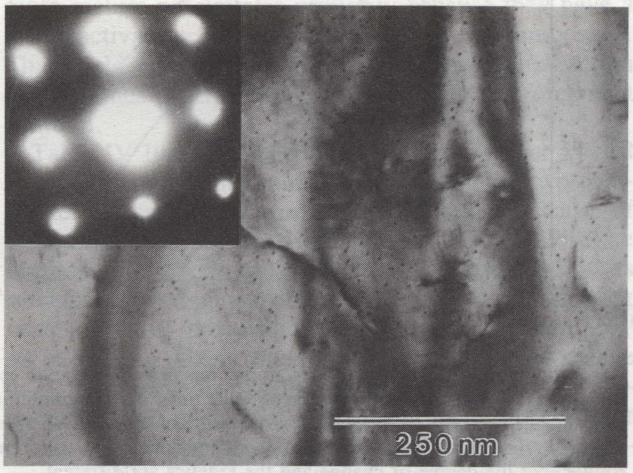

Fig. 15—Bright-field TEM micrograph and the corresponding $[001]_{Al}$ SADP of the matrix of the composite with 10 vol pct Al_2O_3, aged for 300 seconds at 473 K. The density of λ' precipitates is observed to be significantly less than that in the monolith following the same aging treatment (compare with Fig. 7).

of λ' volume fraction and a deceleration of λ' precipitation due to the abundance of vacancy sinks in the composite. Figure 16 shows a reinforcement-matrix interfacial region in the same sample as in Figure 15. In addition to the expected thermally generated dislocations in the matrix next to the alumina reinforcement, several large particles, which were determined by EDXS (energy-dispersive X-ray spectroscopy) to be oxides containing Cu and Mg, are observed at the interface. These interfacial oxides were probably formed during casting, depleting the matrix solute content, and thereby reducing the overall volume fraction of the hardening precipitates. This could be one reason for the lower level of hardening observed in the composites, as compared to the monolithic alloy.

Figure 17 shows the 10 vol pct composite sample after aging for 14,400 seconds at 473 K. A low density of

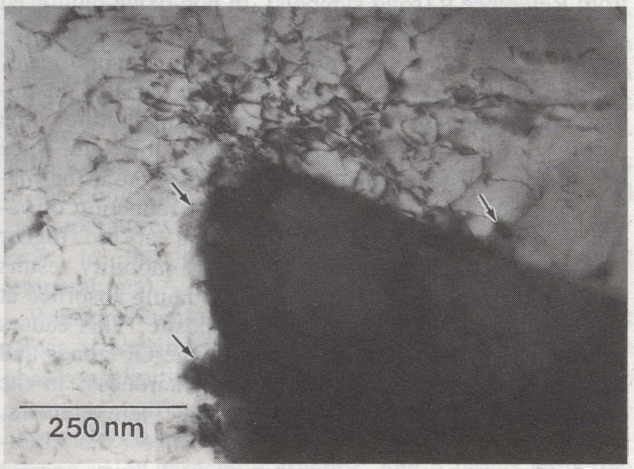

Fig. 16—Bright-field TEM image of a reinforcement-matrix interfacial region in the 10 vol pct composite. Several large particles, which were determined by EDXS to be oxides containing Cu and Mg, are observed at the interface.

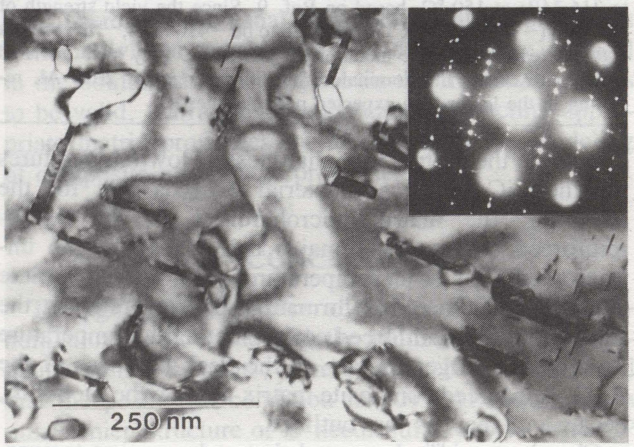

Fig. 17—Bright-field image and the corresponding $[001]_{Al}$ diffraction pattern of the 10 vol pct composite after aging for 14,400 seconds at 473 K. Very thick θ' precipitate plates, as well as some fine needles of λ', are observed.

very thick precipitate plates is observed, with the accompanying SADP identifying these plates as mature θ'. The SADP reveals only two variants of θ' (those with $[001]_{\theta'}$ parallel to $[100]_{Al}$ and $[001]_{Al}$), although the bright-field image clearly reveals the presence of the third variant as well, probably because the selected-area aperture contained only a very few precipitates of this orientation. In addition to the θ' plates, some fine needles of λ' are also observed. Comparing the microstructure in Figure 15 with that of the monolith aged for 14,400 seconds (Figure 9(a)), it is apparent that the dimensions of the λ' needles are comparable, although the θ' plates are much coarser in the composite. This suggests that in the composite, the θ' precipitates, which nucleate heterogeneously at dislocations, are able to grow rapidly *via* pipe diffusion of solute atoms due to the increased matrix dislocation density, and therefore coarsen more rapidly than the precipitates in the monolithic alloy. The λ' precipitates, on the other hand, nucleate at the dissolving GP zones, which are homogeneously distributed in the matrix, and require the diffusion of vacancies for growth. Since vacancies are in short supply in the composite, the λ' needles in the composite are observed to be no coarser than those in the monolith.

IV. DISCUSSION

It is apparent from the results presented in Section III that the presence of alumina particulates significantly influences the precipitation behavior in 2014 Al. During the initial stages of aging of the composite, GP zones nucleate with very short incubation times at the high density of matrix dislocations generated because of CTE mismatch, following which further nucleation occurs at quenched-in vacancy loops. Nucleation at vacancy clusters appears to require longer incubation times, and therefore results in slower GP zone precipitation in the monolith, where the matrix dislocation density is several orders of magnitude lower than that in the composite.[8] In spite of the rapid nucleation of GP zones in the composite, the total volume fraction of the zones formed is clearly reduced because of the presence of reinforcements. This is attributable to a reduction in the concentration of vacancies in the matrix due to absorption at the high density of dislocations in the composites, as well as at reinforcement-matrix interfaces. The decrease in diffusivity due to vacancy absorption at dislocations is also reflected in the reduction of the volume fraction of λ' precipitates in the composites, as well as in the deceleration of λ' formation kinetics. Since λ' evolves from the GP zones, nucleation sites for λ' are abundant. However, λ' formation requires longer-range diffusion than GP zone formation, and therefore, the reduced vacancy concentration in the composites affects precipitation kinetics more adversely for λ' than for GP zones, resulting in the observed deceleration. The nucleation of θ' occurs independently at dislocations, and is accelerated in the composites since the matrix dislocations provide abundant nucleation sites and serve as short-circuit diffusion paths for solute atoms. Because of the close proximity of the θ' precipitates to the dislocations, the kinetics of θ' formation do not seem to be strongly dependent on the matrix vacancy concentration. Indeed, during isothermal aging, commensurate with the reduction in the volume fraction of λ', an increase in both the kinetics and the amount of θ' precipitation is observed (Figure 13).

Peak hardness in 2014 Al at 473 K is associated with the presence of a mixture of λ' and θ' precipitates. Although the presence of reinforcements increases the amount of θ' precipitates somewhat, there is a large reduction in the amount of λ' accompanying it (Figure 13; also compare precipitate densities in Figures 7 and 15). As a result, the increase in hardness that can be achieved *via* aging in alumina-reinforced 2014 Al at 473 K is considerably lower than that in the monolithic alloy, as observed in Figure 1. An additional factor in the lower level of hardening obtained in the composites could be the depletion of Cu and Mg from the matrix to form large oxide particles at the reinforcement-matrix interface during casting (Figure 16). As evident from Table I, the concentrations of both Cu and Mg in the matrix decrease

appreciably with increasing reinforcement volume fraction. It is to be noted that although there may have been slight compositional differences between the control alloy and the matrix alloy of the composites prior to casting, both composites were cast from the same base alloy, and hence, any compositional difference between the two composite matrices following casting is definitely process related. Thus, increasing reinforcement-matrix interfacial area (*i.e.*, increasing volume fraction or decreasing reinforcement size) in Al_2O_3-2014 Al composites results in increased solute depletion from the matrix, thus reducing the overall hardness achievable in the composites. To achieve the same level of hardening in oxide-reinforced MMCs as in monolithic alloys, it may therefore be necessary for the composite matrix alloy to have a larger solute content prior to casting.

As noted earlier, the results of Chawla *et al.*[9] show that at the higher aging temperatures, the level of peak hardness obtained in SiC_p/2014 Al composites is lower than that in the monolith, although at lower temperatures, the composite is harder. This is shown in Figure 18(a), which plots peak hardness data obtained from Reference 9 (solid symbols). In non-oxide-reinforced matrices, solute depletion from the matrix by oxide formation at the interface is not expected to be significant, and the results may be explained on the basis of precipitation mechanisms. At lower aging temperatures, the mobility of the quenched-in vacancies is low, and since the average diffusion distance for absorption at the matrix dislocations can be significant, the reduction of vacancy concentration is less than that at the higher temperatures, where enhanced vacancy mobility results in a larger proportion of the vacancies being absorbed at dislocations or interfaces in the composite. This causes a reduction in the volume fraction of the GP zones and λ', and the consequently lower peak hardness, in the composites at the higher aging temperatures. Figure 18(a) also plots peak hardness data for the Al_2O_3-2014 Al composites used in this study.* It is apparent

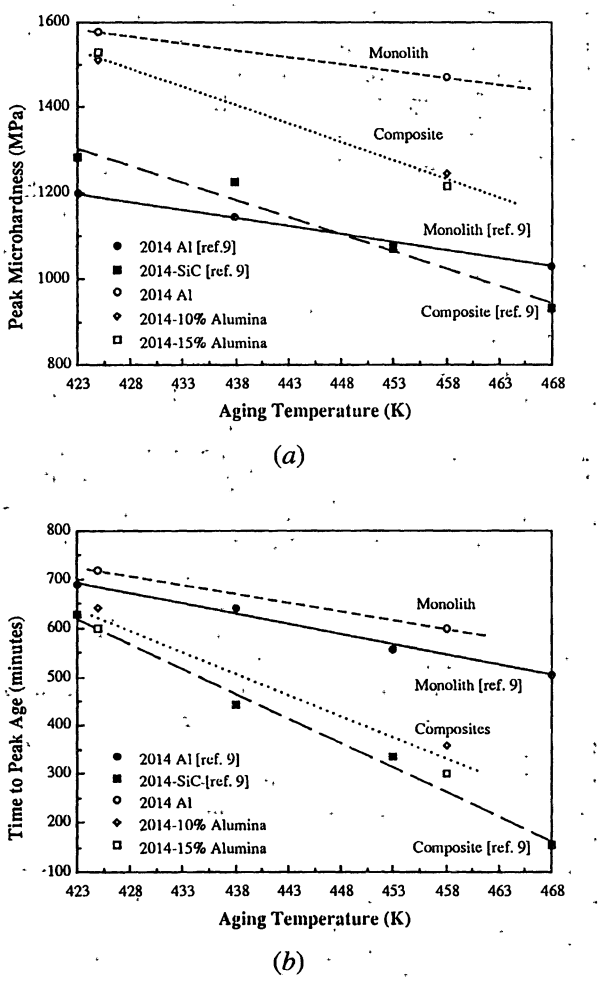

Fig. 18—(*a*) Peak hardness *vs* aging temperature data for monolithic 2014 Al and SiC_p-2014 Al, compiled from Ref. 9. Data for 2014 Al and Al_2O_3-2014 Al from the present investigation are also plotted. (*b*) Time to peak age *vs* aging temperature data for monolithic 2014 Al and SiC_p-2014 Al, compiled from Ref. 9. Data for 2014 Al and Al_2O_3-2014 Al from the present investigation are also plotted.

*Note that the peak hardnesses reported for 2014 Al in Ref. 9 are significantly lower than those found in the present study. Estimating the 0.2 pct offset yield strength (σ_{ys}) from the microhardness (H), using $\sigma_{ys} = H/3\ (0.1)^n$,[26] where n (the strain-hardening exponent) is approximately 0.1 for the peak aged condition, we have, from the present data, σ_{ys} = 417 MPa for the monolith at 152 °C, as compared to 316 MPa at 150 °C, based on Ref. 9. Since the yield strength of 2014-T6 (~18 h at 160 °C) is expected to be ~410 MPa,[27] the present data are reasonable. The material used in Ref. 9 may have deviated significantly from the nominal composition range for 2014 Al, resulting in the lower-than-expected peak hardnesses.

that while the matrix microhardness at low temperatures for the SiC-reinforced material exceeds that for the monolith, the matrix microhardness of the Al_2O_3-reinforced composites remains below that for the unreinforced alloy at all temperatures, as a result of solute depletion due to oxide formation. However, as in the case of the SiC-reinforced composite, aging temperature does have a larger impact on the peak hardness of the Al_2O_3-reinforced composite matrix than on the monolith, because of reasons just outlined.

Chawla *et al.*[9] also noted that at low aging temperatures, the overall hardening kinetics of the composite and the monolith are similar, but at higher temperatures, the composite shows accelerated aging. This observation is consistent with the results of the present study, data from which are superimposed on data from Reference 9 in Figure 18(b). The peak-hardened condition in 2014 Al corresponds to a mixed microstructure containing λ' and θ' precipitates, with the proportion of λ' decreasing (*i.e.*, the proportion of θ' increasing) with increasing temperature.[16] At low temperatures, the aging kinetics are dominated by the kinetics of λ' precipitation, which require vacancy diffusion, and even a modest decrease in the vacancy concentration is likely to slow λ' precipitation substantially. Therefore, despite the abundance of dislocations in the composite matrix, not much overall acceleration of hardening is noted at low temperatures. At higher temperatures, on the other hand, there is a large contribution from θ' precipitates, which form on dislocations, their growth rate being determined by solute diffusivity along dislocation cores. With increasing temperatures, the paucity of vacancies in the composite matrix (and the consequently slower λ' precipitation) is offset by an enhanced pipe diffusivity, resulting in a significant enhancement in the rate of θ' precipitation, and

therefore, the overall hardening kinetics. This rationalization is consistent with the activation energy data in Table IV, which clearly show that E_a for λ' precipitation is larger in the composites than in the monolith, whereas E_a for θ' precipitation is smaller in the composites relative to the monolith. Therefore, the hardening kinetics of the composite matrix are apt to be more accelerated at temperatures where the contribution of θ' is relatively large to the peak hardness (*i.e.*, at high aging temperatures).

Reinforcement with alumina particulates, thus, has the effect of altering the hardening kinetics, as well as the phase constitution of the peak-aged alloy. In general, the enhanced matrix dislocation density in the composite favors the formation of θ' over λ', resulting in greater acceleration of hardening kinetics, and a larger reduction in the peak hardness relative to the unreinforced alloy, with increasing aging temperatures. Because of this, as well as the depletion of solute *via* the formation of interfacial oxides, the properties of the peak-aged matrix alloy in combination with alumina reinforcements may be substantially different from those of the unreinforced matrix. Therefore, the usual assumption that the properties of the individual constituents of a composite are identical in the combined form to those in the free state, ceases to be valid, warranting special care in selecting appropriate matrix properties for use in predictive modeling of composite mechanical properties.

V. CONCLUSIONS

The aging characteristics of commercial 2014 aluminum alloy, without and with the addition of alumina particulate reinforcements, were studied. It was confirmed that the peak-aged condition in 2014 Al consists of a mixed microstructure of λ' needles that evolve from GP zones forming at quenched-in vacancy clusters, and θ' platelets that form primarily on matrix dislocations. The addition of 10 vol pct alumina particulates significantly altered the kinetics and amounts of the various precipitates that form in 2014 Al during aging, with further additions having a progressively smaller effect. Reinforcement addition accelerated the kinetics of GP zone and θ' precipitation, while decelerating the kinetics of λ' formation. Because of the acceleration of θ' formation, the overall hardening kinetics of the composites were observed to be accelerated relative to the monolith. Alumina addition also decreased the volume fraction of λ' formed and thus resulted in a lower peak matrix microhardness than in the monolithic alloy. The acceleration in aging was attributable primarily to enhanced precipitate nucleation at thermally generated dislocations, as well as pipe-diffusion-enhanced growth of θ', whereas the reduction in peak hardness was attributable to a reduced vacancy concentration in the composite matrix due to absorption at dislocations and interfaces. Both the acceleration of aging and the reduction of peak hardness with reinforcement addition were greater at higher temperatures. The increased acceleration of hardening kinetics in the composites with increasing temperatures was attributed to the favorable impact of the enhanced dislocation density in the MMCs on θ' formation, which predominates in the peak-hardened microstructure at the higher aging temperatures. The larger reduction in peak hardness at higher temperatures, on the other hand, was attributed to the larger reduction in the amount of λ' precipitated in the composite with increasing temperature, relative to the monolith, because of the reduced matrix vacancy concentration. An additional, temperature-independent contribution to the reduction in peak hardness of the composite matrices was found to arise because of solute depletion from the composite matrix by the formation of interfacial oxides during fabrication. Because of the changes in the relative proportions of λ' and θ' formed, as well as solute depletion during processing, the peak-aged matrix alloy in the reinforced condition is expected to possess mechanical properties which are appreciably different from those of the free, unreinforced alloy.

ACKNOWLEDGMENTS

This work was supported by funds administered by the Naval Postgraduate School Research Council. The authors are grateful to Mr. Charles T. Lane of Duralcan, Inc., for supplying the cast composites used in this work.

REFERENCES

1. T.G. Nieh and R.F. Karlak: *Scripta Metall.*, 1984, vol. 18, pp. 25-28.
2. R.J. Arsenault and R.M. Fisher: *Scripta Metall.*, 1983, vol. 17, pp. 67-71.
3. I. Dutta, D.L. Bourell, and D. Latimer: *J. Compos. Mater.*, 1988, vol. 22, pp. 829-49.
4. T. Christman, A. Needleman, and S. Suresh: *Mater. Sci. Eng.*, 1989, vol. A107, p. 49.
5. I. Dutta and D.L. Bourell: *Mater. Sci. Eng.*, 1989, vol. A112, pp. 67-77.
6. T. Christman and S. Suresh: *Acta Metall.*, 1988, vol. 36, pp. 1691-1704.
7. J.M. Papazian: *Metall. Trans. A*, 1988, vol. 19A, pp. 2945-53.
8. I. Dutta, S.M. Allen, and J.L. Hafley: *Metall. Trans. A*, 1991, vol. 22A, pp. 2553-63.
9. K.K. Chawla, A.H. Esmaeili, A.K. Datye, and A.K. Vasudevan: *Scripta Metall.*, 1991, vol. 25, pp. 1315-19.
10. I. Dutta and D.L. Bourell: *Acta Metall.*, 1990, vol. 38, pp. 2041-49.
11. C.M. Friend and S.D. Luxton: *J. Mater. Sci.*, 1988, vol. 23, pp. 3173-80.
12. S. Suresh, T. Christman, and Y. Sugimura: *Scripta Metall.*, 1989, vol. 23, pp. 1599-1602.
13. J. Crowther: *J. Inst. Met.*, 1949–50 vol. 76, pp. 201-36.
14. G. Phagrem: *J. Inst. Met.*, 1950, vol. 77, pp. 489-551.
15. H.W.L. Philips: *Equilibrium Diagrams of Aluminium Alloy Systems*. The Aluminum Development Association, London, 1961, pp. 128-33.
16. B. Dubost, J. Bouvaist, and M. Reboul: *Proc. Int. Conf. on Aluminum Alloys*, Charlottsville, VA, 1986, vol. II, pp. 1109-23.
17. W. Bonfield and P.K. Datta: *J. Mater. Sci.*, 1976, vol. 11, pp. 1661-66.
18. W. Bonfield and P.K. Datta: *J. Mater. Sci.*, 1977, vol. 12, pp. 1050-52.
19. J.M. Silcock: *J. Inst. Met.*, 1960, vol. 89, pp. 203-10.
20. G.C. Weatherly and R.B. Nicholson: *Phil. Mag.*, 1968, vol. 17, p. 813.

21. J.M. Papazian: *Metall. Trans. A*, 1981, vol. 12A, pp. 269-80.
22. A.A. Frost and R.G. Pearson: *Kinetics and Mechanisms*, John Wiley and Sons, New York, NY, 1961, p. 77.
23. P.N. Adler and R. DeIasi: *Metall. Trans. A*, 1977, vol. 8A, pp. 1185-90.
24. J.A. Augis and J.E. Bennett: *J. Therm. Anal.*, 1978, vol. 13, p. 283.
25. H. Yinnon and D.R. Uhlmann: *J. Non-Cryst. Solids*, 1983, vol. 54, pp. 253-75.
26. G.E. Dieter: *Mechanical Metallurgy*, 2nd ed., McGraw-Hill, New York, NY, 1976.
27. *Metals Handbook, vol. 2, Properties and Selection: Nonferrous Alloys and Special-Purpose Materials*, 10th ed., ASM INTERNATIONAL, Metals Park, OH, 1990.